

# Impact of an invasive species, *Crepidula fornicata*, on the hydrodynamics and transport properties of the benthic boundary layer

Frédéric Y. Moulin<sup>1,a</sup>, Katell Guizien<sup>2</sup>, Gérard Thouzeau<sup>3</sup>, Georges Chapalain<sup>3</sup>, Karen Mülleners<sup>1</sup> and Catherine Bourg<sup>1</sup>

<sup>1</sup> Institut de Mécanique des Fluides de Toulouse (IMFT), UMR 5502, 1 allée du Professeur Camille Soula, 31400 Toulouse, France

<sup>2</sup> Université Pierre et Marie Curie-Paris 6, CNRS UMR 7621, 66650 Banyuls-sur-Mer, France

<sup>3</sup> UMR 6539 CNRS – LEMAR, Institut Universitaire Européen de la Mer, Place N. Copernic, 29280 Plouzané, France

Received 27 October 2006; Accepted 30 March 2007

**Abstract** – We investigated the impact of an invasive species, *Crepidula fornicata* on the hydrodynamics and transport properties of the benthic boundary layer. We present results obtained by three different approaches: 1) in-situ measurements of near-bottom current and suspended sediment concentration on two sites in the Bay of Brest (Brittany, France), 2) velocity measurements in controlled laboratory experiments of flows over a bed of artificial *Crepidula* shells, and 3) numerical simulations of the flow over two-dimensional shell-like bed forms. Numerical and laboratory experiments showed that both the bed erosion and the exchange velocity between the canopy and the outer flow decrease as the roughness density increases. These results suggest a sheltering effect by the *Crepidula* shells increasing with the surface density of shells. This trend was also found in field measurements: during spring tides, higher particle resuspension was observed on the muddy sand bottom with few chains of slipper limpets compared with the high-density area. However, other processes may explain these data; their importance is thus discussed in this study.

**Key words:** Benthic boundary layer / Biogenic roughness / Transport / Turbulence / Erodability

**Résumé** – Impact d'une espèce invasive, *Crepidula fornicata*, sur l'hydrodynamique et les propriétés de transport de la couche limite benthique. Nous avons étudié l'impact d'une espèce invasive, *Crepidula fornicata*, sur l'hydrodynamique et les propriétés de transport de la couche limite benthique. Nous présentons les résultats obtenus au moyen de trois approches différentes : 1) des mesures in-situ du courant près du fond et de la concentration de sédiment en suspension sur deux sites en Baie de Brest (Bretagne, France), 2) des mesures de vitesse dans des expériences contrôlées en laboratoire d'écoulements au-dessus de coquilles artificielles de *Crepidula*, et 3) des simulations numériques d'un écoulement au-dessus d'un fond bidimensionnel en forme de coquilles. Les simulations numériques et les expériences de laboratoire ont montré que l'érosion du lit et la vitesse d'échange entre la canopée et l'écoulement externe décroissaient lorsque la densité en coquillages augmentait. Ces résultats suggèrent un effet de protection par les coquilles de *Crepidula* dont l'efficacité croît avec la densité en coquillages. Cette tendance a été également trouvée dans les mesures de terrain : durant les marées d'équinoxe, la resuspension observée sur le fond de sable fin envasé faiblement colonisé par les crépidules est plus importante que sur le site à forte densité en crépidules. Néanmoins, d'autres processus peuvent expliquer ces données ; leur importance est donc discutée dans cette étude.

## 1 Introduction

The American slipper limpet *Crepidula fornicata* is a gastropod mollusk that can tolerate a wide range of environmental conditions. This invasive species has now spread through large parts of Europe and can be observed from the Baltic Sea to the French Atlantic coast of the Mediterranean sea (Blanchard 1997). Populations are particularly well developed

in sheltered and shallow areas as bays or estuaries and the proliferation phenomenon is still going on. In the Bay of Brest, the species has been first introduced during Allied shipping operations from Great Britain or directly from the USA. A second massive importation occurred during the 1970's, together with the introduction of Japanese oyster (*Crassostrea gigas*) spat from Japan and the west coast of the USA. Slipper limpet proliferation really started in the mid-eighties to reach ca. 125 000 tons wet weight in the year 2000 (Guérin 2004). Some impacts of this invasion have been clearly identified.

<sup>a</sup> Corresponding author: moulin@imft.fr

First, the increasing proliferation of the slipper limpet has negative socio-economic consequences on scallop and oyster farming (Blanchard 1997) and coastal fishing activities are endangered because heavily-impacted areas become unfit for commercial exploitation (Thouzeau et al. 2000, 2003; Frésard and Boncoeur 2006). Second, decreases in phytoplanktonic primary production (Chauvaud et al. 2000) and biodiversity of the benthic macrofauna have been observed (Chauvaud 1998; Thouzeau et al. 2000, 2003). Third, the species has been reported to modify the texture of the colonized grounds leading to an overall sediment silting. These changes are partly due to filtration activity and biodeposits production (feces and pseudofeces). However, sediment changes may also result from roughness changes due to the shells on the bottom, that modify both the structure and mixing properties of the boundary layer above. This is the latter issue that is addressed in the present paper.

Recent studies focused on the impact of the American slipper limpet on biogeochemical cycles in the Bay of Brest, like its role as an active coastal silicate pump (Chauvaud et al. 2000; Ragueneau et al. 2002, 2005; Martin et al. 2006; Martin et al. in press). Since this species becomes a major actor of the ecosystem in the invaded areas, its metabolism has been intensively studied by *in situ* and laboratory measurements (Richard 2005; Martin et al. 2006; Martin et al. in press). All these studies provide results valid for a large-scale description of the biological and chemical fluxes obtained through a spatial averaging that does not take explicitly the hydrodynamic conditions into account. The importance of the hydrodynamic forcing has been illustrated recently by field measurements of  $O_2$  turbulent fluxes (Berg et al. 2003). The authors showed that the measurements with benthic chambers underestimate the real fluxes. Values are lower in the laminar or low-energetic flows of the benthic chambers than in high Reynolds turbulent boundary layers. Coupling the near-bottom processes, like the production of dissolved and particulate matter by individual slipper limpets, with the hydrodynamic conditions that control the large-scale spatially-averaged fluxes, becomes essential when one investigates the impact of this species on the transport of particulate matter.

The near-bottom boundary layer over rough surfaces has been already studied in a very wide range of contexts. In river flows, early studies addressed the hydraulic roughness of natural beds, ranging from fine sand to large pebbles (Kamphuis 1974; Bayazit 1976). Recently, studies focused on the change of hydraulic roughness driven by biofilm growing at the bottom, and its feedback on the fluxes of nutrients available for the biofilm (Godillot et al. 2001). In coastal engineering, the shoreline stability is a major issue that led to numerous studies of sediment transport within the rough bottom boundary layer, and in particular studies on the hydraulic roughness changes driven by wave-current interactions (Kemp and Simons 1982; Kemp and Simons 1983; Fredse et al. 1999). In the atmospheric boundary layer, the coupling of near-bottom processes with the flow above arises when one investigates the impact of photosynthesis and respiration of vegetal canopies on large-scale  $CO_2$  and  $O_2$  bottom fluxes (Kitaya et al. 2004), or when one studies the dispersion of pollutants in urban canopies (Kastener-Klein et al. 1997). In the

context of the structure and functioning of coastal ecosystems, few researchers studied the coupling between biological and hydrodynamic processes (Gaylord et al. 2004 for macroalgae or Crimaldi et al. 2002 for clams). Within this wide range of applications, the more advanced works are found in the atmospheric, river and coastal engineering fields. On the one hand, river and coastal engineers proposed early values for the hydraulic roughness and displacement thickness for the inertial part of turbulent boundary layers over natural beds (Kamphuis 1974; Bayazit 1976). Then, time- and spatially-averaged currents over 2D sedimentary bedforms with wave-current interaction were studied by laboratory experiments or numerical simulations to provide values of the hydraulic roughness and displacement thickness. However, all these studies focused on the modified flow far above the roughness, disregarding the flow below the top of the rough elements. On the other hand, atmosphericists applied successfully similar descriptions for the spatially-averaged flow in turbulent boundary layers over surfaces with three-dimensional cubic or rectangular elements (McDonald 2000; Cheng and Castro 2002; Castro et al. 2006; Coceal et al. 2006). They also added a description for the flow inside the canopy layer, i.e. between the bottom and the top of the obstacles. Moreover, attempts have been made recently to extend this purely hydrodynamical modelling to the transport of matter (dissolved or in suspension) between the canopy and the flow above (Bentham and Britter 2003; Hamlyn and Britter 2005). Yet, the effect of natural large obstacles on the transport of solid matter is still a widely open question whose nearest issue seems to be the problem of scour in civil engineering, a local enhancement of the bottom shear stress induced by the presence of an obstacle (Hughes and Schwichtenberg 1998).

In the present paper, we investigate the impact of the invasive suspension-feeding mollusk species, *Crepidula fornicata* on the hydrodynamic and transport properties of the benthic boundary layer. Mean turbulent quantities are considered here, but the time-averaging procedure is done on time-scales small enough to provide a description of the evolution of the bottom boundary layer properties during a tidal cycle.

Our results could be relevant for other biological substrates. Since this question requires a better understanding of the coupling between the very near-bottom processes and the turbulent boundary layer above, three complementary methodological approaches were adopted: (i) a field survey carried out in the Bay of Brest on two different sites along a density gradient of slipper limpets, (ii) an experimental study of the flow near artificial molds of limpets performed in a laboratory flume, and (iii) numerical simulations of the turbulent boundary layer above a bed covered with two-dimensional (2D) limpet-like obstacles. The theoretical background is presented at the beginning of the Material and Methods section. Our results are compared to existing analytical models for the mean velocity profiles and the exchange velocity from the canopy layer. The relevance of such simple analytical models to study sediment stability between the shells is discussed. The trends in density-dependent bed erosion and exchange velocity are confronted to the field measurements. The limitations of such a comparison are highlighted and yield a discussion of the other processes that deserve particular attention in future investigations.

## 2 Material and methods

### 2.1 Theoretical background: mean velocity profile, exchange vertical velocity, bed erosion

Although an incompressible turbulent flow instantaneously satisfies the Navier-Stokes equations, it is difficult to predict the flow in detail. Fortunately the distribution of the mean velocity is generally of greater interest than the distribution of the instantaneous velocity. Therefore the motion is decomposed into a mean state plus turbulent fluctuations. Mean quantities are calculated based on the Reynolds decomposition:

$$u = \bar{u} + u', \quad v = \bar{v} + v' \quad \text{and} \quad w = \bar{w} + w' \quad (1)$$

where a bar is used to indicate the mean state and a prime to indicate the turbulent part. The equations describing the mean flow are found by substituting the Reynolds decomposition (1) into the instantaneous Navier-Stokes equations and time-averaging them. In the so-called Reynolds Averaged Navier-Stokes (RANS) equations, six additional unknowns, namely the components of the Reynolds turbulent stress tensor (turbulent fluctuations correlation matrix), appear, that act on the mean flow. The simplest available turbulence closure for boundary layer flows combines the Boussinesq eddy-viscosity approximation and Prandtl mixing-length theory (Prandtl 1925). Using these assumptions and introducing the adimensional vertical coordinate  $z^+ = zu_*/\nu$  where  $u_* = \sqrt{-(\overline{u'w'} + \overline{v'w'})}/\rho$  is the so-called friction velocity, the free stream mean flow near a flat smooth bed can be described by three-layers: a viscous sublayer for  $0 < z^+ < 10$  where the diffusive transport of momentum is dominant, a buffer layer for  $10 < z^+ < 30$ , and a log-law layer ( $30 < z^+ < 600$ ) where the vertical flux of momentum is completely driven by the turbulent fluctuations and yields a solution reading  $\bar{u}/u_* = (1/\kappa)\ln(z^+) + 5.5$  with  $\kappa = 0.41$  (von Kármán constant). In flows above a flat rough bed, the boundary layer description simplifies to the sole log-law layer where the velocity reads:  $\bar{u}/u_* = (1/\kappa)\ln(z/z_0)$  with  $z_0$  the roughness length.

By extension, in flows above urban and vegetal canopies or any natural large roughness like the one we study here, the structure of the boundary layer can be described by two layers (see Cheng and Castro 2002): the roughness sublayer (RS), which extends beyond the top of the rough elements and where the flow is still influenced by individual elements, and the inertial sublayer (IS) above, where the flow is horizontally homogeneous. In the IS, a log-law vertical profile of horizontal velocity  $\bar{u}$  still exists for  $z$  ranging from 0 to  $0.2\delta$  where  $\delta$  is the boundary layer thickness. However, the origin of the vertical coordinate for this law is unknown and must be prescribed through an additional parameter, the displacement thickness  $d$ , defining the plane where the surface drag acts (see Jackson 1981 for physical arguments supporting this idea). Then, the mean velocity profile in the inertial (or log-law) layer reads

$$\frac{\bar{u}}{u_*} = \frac{1}{\kappa} \ln\left(\frac{z-d}{z_0}\right) \quad (2)$$

where  $z = 0$  is located at the bottom of the rough elements.

When entering the RS, the mean flow becomes gradually three-dimensional with depth. The lowest part of the RS is called the canopy layer (CL) and has a depth equal to the mean obstacle height  $H$ . By a horizontal spatial averaging of the flow components (denoted with angle brackets  $\langle \cdot \rangle_{xy}$ ), it is still possible to obtain vertical profiles of the mean spatially averaged longitudinal velocity  $U(z) = \langle \bar{u}(x, y, z) \rangle_{xy}$ . In recent studies (McDonald 2000; Cheng and Castro 2002), the mixing-length theory has been applied to these spatial and time-averaged flow components, yielding analytical solutions in good agreement with experimental measurements for cubic obstacles. In particular, the flow in the lowest part of the RS exhibits an exponential behavior that reads:

$$\bar{u}(z) = \bar{u}(H) \exp\left[a\left(\frac{z}{H} - 1\right)\right]. \quad (3)$$

The behaviour of the flow in the RS depends mainly on the planar density of the roughness elements,  $\lambda_p$ , and on the frontal density of the roughness elements  $\lambda_f$  (McDonald 2000). The parameters  $d$  and  $z_0$  that appear in the flow description in the IS are prescribed by the flow in the RS, and therefore also depend on  $\lambda_p$  and  $\lambda_f$ .

With this complete description of the time- and spatially-averaged flow from the bottom to the IS, previous studies proposed models to predict the vertical exchange of dissolved or suspended matter between the free stream and the canopy layer (Bentham and Britter 2003; Hamlyn and Britter 2005). In the work of Bentham and Britter (2003), a reference velocity, noted  $U_{\text{ref}}$ , was chosen at  $z = 2.5H$ , i.e. at the beginning of the inertial sublayer, and a canopy velocity  $U_c$  was defined by:

$$U_c^2 = \frac{1}{H} \int_0^H \bar{u}(z)^2 dz. \quad (4)$$

The latter definition is related to the fact that the bottom friction is mainly due to the flow around the shells, and scales therefore as  $\bar{u}^2$  for values of the local Reynolds number high enough. Then, an exchange velocity of horizontal momentum between the two regions of the flow,  $U_E$ , is defined by:

$$u_*^2 = U_E(U_{\text{ref}} - U_c). \quad (5)$$

With the assumption of a turbulent Schmidt number close to unity near the crests of the rough elements, the flux of substances between the canopy region and the flow above is controlled exactly by the same exchange velocity  $U_E$ . Therefore, if we denote  $c_C$  the concentration of a particular substance in the canopy region, and  $c_{\text{ref}}$  its concentration at the reference height  $z = 2.5H$ , the vertical flux of this substance from the canopy region towards the flow above reads:

$$\Phi_{\text{mass}} = U_E(c_C - c_{\text{ref}}). \quad (6)$$

Yet, to deal with fluxes of dissolved matter from the sediments, or fluxes of sediments themselves, some condition must be prescribed for the flux at the lower boundary, i.e. at the bottom of the roughness sublayer. These fluxes are not directly related to the turbulence of the IS but are controlled by the components of the turbulent stress in the limit  $z \rightarrow 0$ . As a consequence, whereas the external flow experiences a drag measured by the

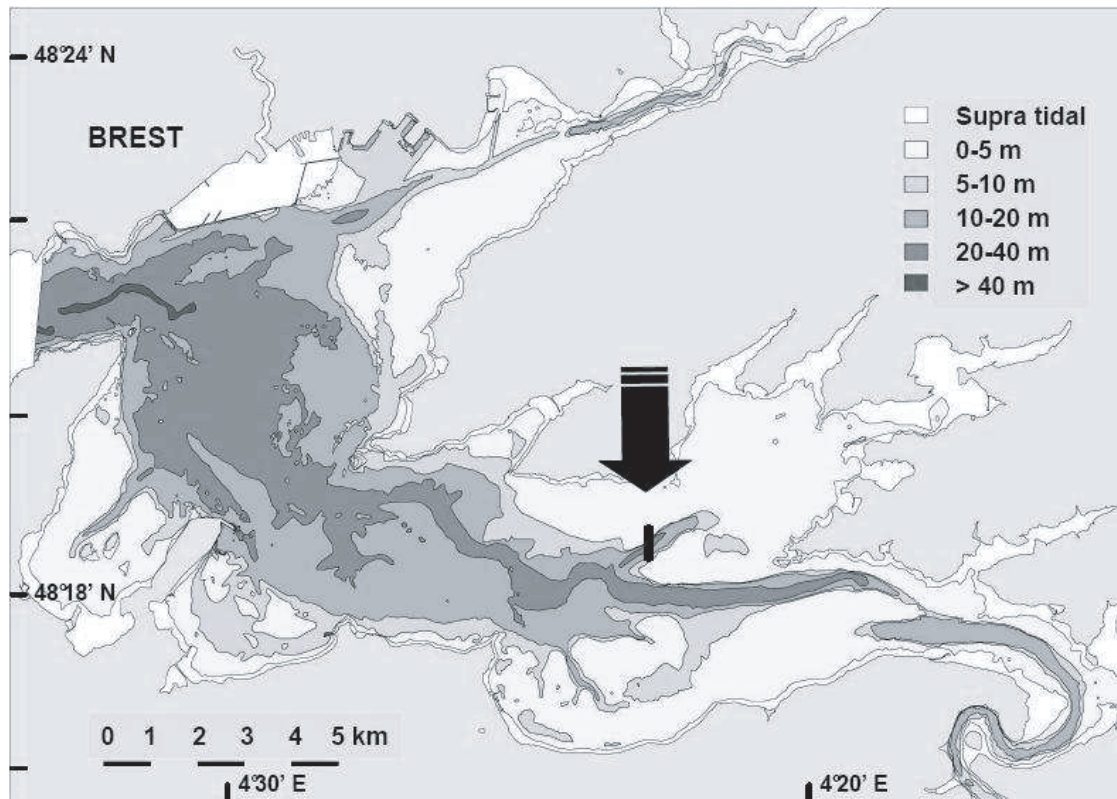


**Fig. 1.** Bathymetry and location of the two study sites (S1, S2, 18 m and 3 m depth, respectively) selected for the field survey in the Bay of Brest. See the Method section for geographical coordinates of the two study sites. The latter are located along a north-south transect (black plain line) perpendicular to the axis of the main tidal current in the southern basin of the bay.

friction velocity  $u^*$  (which is the sum of the drag driven by the flow around the obstacles and of the skin drag to a lesser extent), the transport of solid matter at the bottom is controlled by the skin drag only. In the following, we denote  $\tau_b$  the averaged bottom shear stress, and  $\tau_H$  the horizontally averaged shear stress measured at the top of the shells:

$$\tau_b = \rho \langle (\overline{u'w'^2} + \overline{v'w'^2})^{1/2} \rangle_{xy} (z \rightarrow 0)$$

$$\tau_H = \rho \langle \overline{u'w'} \rangle_{xy} (z = H).$$

The issue is then to predict, for a given distribution of roughness elements, which proportion of the total drag contributes to the transport of solid matter. This is measured by the ratio  $\tau_b/\tau_H$  which depends on the distribution and the shape of the obstacles.

## 2.2 Field surveys

The Bay of Brest is a shallow marine ecosystem located at the extreme West of France. The hydrodynamics of the bay is forced by the tides and to a lesser extent by river inputs from two main rivers, the Aulne and Elorn. More than half of the benthic surface area is colonized by *Crepidula fornicata* (Guérin 2004). The colonization is not homogenous spatially due to aggregative distribution. Highest slipper limpet densities are found in the southern basin (up to 4600 ind  $m^{-2}$  for

a biomass of 7.5 kg wet weight  $m^{-2}$ ) while the mean density at the bay scale is about 260 ind  $m^{-2}$  (Guérin 2004). From previous studies on flows over roughness elements (McDonald 2000), it is well known that the density of identical rough elements is one of the most relevant parameter to describe the flow. Therefore, two sites with contrasted *C. fornicata* densities were chosen for the field survey: site S1 (48°18'604 N, 4°23'207 E; 18 m depth) with more than 1500 ind  $m^{-2}$ , and site S2 (48°18'728 N, 4°23'387 E; 3 m depth), about 300 m apart, with a density lower than 50 ind  $m^{-2}$  (Fig. 1). A bottom-landing water sampling system (Bale and Barrett 1995) was deployed in each site over complete tidal cycles. This sampler enables vertical profiles of water samples to be obtained within the benthic boundary layer. A maximum of ten samples spread over 2 m immediately above the seabed can be obtained on each deployment: two vertical masts located within the centre of a 2.4 m high pyramid frame carry an array of ten horizontally mounted sampling bottles (10 L Teflon® coated Niskin bottles). In this study, water samples were collected at 20, 40, 60, 100, 140 and 200 cm off the bottom. The design of the sampling bottles minimizes the disturbance due to particle aggregates and positive displacement sampling ensures that the samples are representative of the environment (Bale and Barrett 1995). A control cylinder senses the frame altitude and initiates the bottle closing mechanism after a 2 min pre-set delay, thus preventing possible sediment resuspension induced by the frame landing to alter sample

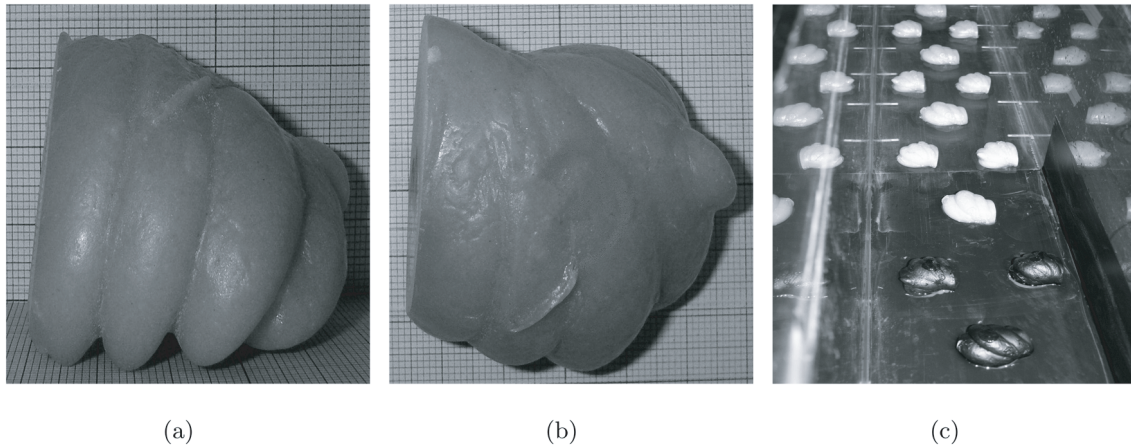


**Fig. 2.** (a) Front and (b) top view of a mold (number 1, Table 1) made of real shells and chains of the slipper limpet *Crepidula fornicata*. (c) Photography of the molds attached to the bottom of the hydraulic flume in B configuration.

**Table 1.** Overview of the height ( $H$ ), the volume ( $V$ ) and the frontal area ( $A_f$ ) of the eight different shell molds.

Mold n°	1	2	3	4	5	6	7	8
$H$ [cm]	$4.2 \pm 0.2$	$3.2 \pm 0.2$	$3.4 \pm 0.2$	$3.1 \pm 0.2$	$3.0 \pm 0.2$	$3.1 \pm 0.2$	$2.7 \pm 0.2$	$2.6 \pm 0.2$
$A_f$ [cm <sup>2</sup> ]	$25.1 \pm 0.5$	$18.7 \pm 0.5$	$15.4 \pm 0.5$	$14.5 \pm 0.5$	$13.6 \pm 0.5$	$13.1 \pm 0.5$	$9.8 \pm 0.5$	$9.5 \pm 0.5$
$V$ [cm <sup>3</sup> ]	$55 \pm 3$	$45 \pm 3$	$40 \pm 3$	$40 \pm 3$	$35 \pm 3$	$32 \pm 3$	$25 \pm 3$	$21 \pm 3$

quality. Two surveys were conducted with the R.V. *Côtes de la Manche* on September 2005 and April 2006. Water samples were collected over a 12 h period in each study site in September 2005 and April 2006. The sampling frequency was 90 min that are 9 sampling times per tidal cycle.

Horizontal current velocity measurements in the lower part of the bottom boundary layer were also performed during the survey of April 2006, using acoustic VECTOR (NORTEK®) current meters mounted at 10 and 40 cm above the bottom on a stem stuck in the seabed. Nine minutes long sequences were acquired every 30 min at a sampling rate of 8 Hz. Values of the friction velocity were deduced from the quantity  $(\overline{u'w'^2} + \overline{v'w'^2})^{1/2}$ , with  $u'$ ,  $v'$  the horizontal velocity fluctuations and  $w'$  the vertical velocity one. At 40 cm above the bottom, the turbulent quantities do not reflect anymore the horizontal distribution of bottom rugosities, and the quantity  $(\overline{u'w'^2} + \overline{v'w'^2})^{1/2}$  is close to its horizontally-averaged value at the bottom (in other words, measurements are done in the lower part of the turbulent boundary layer).

Water samples were filtered on pre-combusted pre-weighted 47-mm glass fibre GF/F filters ( $0.7 \mu\text{m}$ ) on board the ship and filters were stored at  $-20^\circ\text{C}$  until the time of analysis. At the laboratory, samples were dried at  $60^\circ\text{C}$  for 48 h and weighted (dry wt; 0.001 g) to obtain total suspended particulate matter (SPM) concentrations. Then, filters were burned for 4 h at  $450^\circ\text{C}$  and weighted again to calculate the inorganic fraction in SPM. The organic fraction was deduced from the difference between the total and inorganic fractions. The particle isoconcentration contours were obtained by kriging interpolation (SURFER® software; spherical variogram model).

### 2.3 Experiments in a laboratory flume

During the field surveys in the Bay of Brest, eight representative chains of *Crepidula fornicata* were collected, dried, and used to produce plastic molds with a good reproduction of even the smallest details of the shells (Fig. 2). The molds have an average height of  $H = 3.2$  cm and are about 5 cm wide. Exact heights of the eight numbered molded chains are given in Table 1, as well as their frontal area, i.e. the area exposed to the flow,  $A_f$  as defined by McDonald (2000), and their volume  $V$ . Experiments were performed in a 20 m long, 0.2 m wide hydraulic flume. The shell molds were attached to the bottom of the flume (Fig. 2c) in three different regular configurations (Fig. 3) that corresponded approximatively to field densities of 150, 450 and 900 ind  $\text{m}^{-2}$  for configurations A, B and C. Values of the frontal densities  $\lambda_f = A_f/A_d$ , where  $A_d$  is the underlying surface area of an obstacle (total area divided by the number of obstacles), for the three configurations A, B, and C were equal to  $\lambda_f = 0.05$ ,  $\lambda_f = 0.12$  and  $\lambda_f = 0.24$ . Replicated configuration units of  $20 \times 20 \text{ cm}^2$  were used to provide a periodic pattern used in the horizontal spatial averaging procedure described below.

Identical external flow conditions were chosen for all the experiments presented in this study, with a water depth  $D = 30$  cm and a volumic fluid flux  $Q = 20 \text{ L s}^{-1}$ , yielding values of the free stream velocity,  $U_\infty$ , around  $40 \text{ cm s}^{-1}$ , a typical value for tides in the Bay of Brest. Indeed, the structure and properties of the turbulent boundary layer are known to be independant of the Reynolds number  $Re = HU_c/\nu$ , with  $H$  the height of the rough elements,  $U_c$  the velocity at the level of the rough elements and  $\nu$  the kinematic viscosity, for values of  $Re = HU_c/\nu$  large enough (i.e. over 1000, Cheng and Castro 2002). In our experiments, we checked that the values

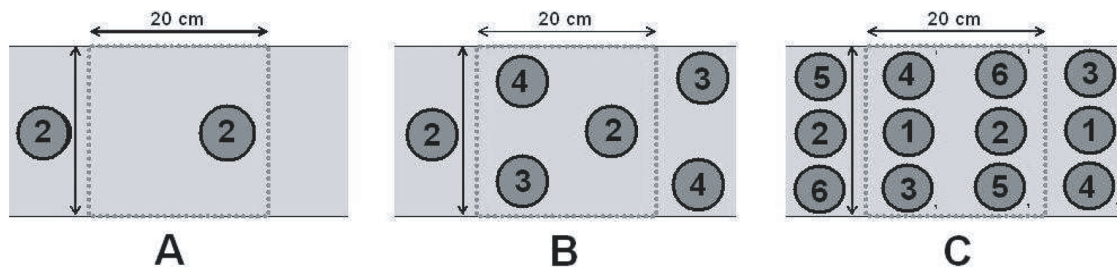


**Fig. 3.** Schematic representation of the three experimental shell (A, B, C) configurations. The numbers indicate which of the eight different shell molds is used.

of the Reynolds number were always larger than this lower limit. Therefore, the turbulent boundary layers developed in the flume exhibited the same characteristics as in the wild.

The measurement section is located 10 m downstream of the hydraulic flume entrance. In this region the flow and the turbulent boundary layers are fully developed, i.e. the height of the bottom turbulent boundary layer  $\delta$  does not grow anymore. It should be noted that the thickness of the bottom boundary layer is not equal to the water depth  $D$ , because of the lateral boundary layers. Indeed, the vertical depth of the developed bottom boundary layer increases with the density of shells that enhances the hydraulic roughness of the bottom plane. Nevertheless, the flow structure near the rough elements is expected to be weakly influenced by the thickness of this boundary layer and to depend essentially on the value of the friction velocity and the distribution of shells. Velocity measurements were carried out using a Particle Image Velocimetry (PIV) technique, with algorithms developed by Fincham and Delerce (2000) to calculate the velocity field from image pairs.

The variables in a turbulent flow are not deterministic in detail and have to be treated as stochastic or random variables. Therefore the Reynolds decomposition (1) is applied and mean quantities are obtained through a time-averaging procedure. For reasonable statistical convergence of the time-averaged quantity, a large number of samples is required. Velocity components  $u$ ,  $v$  and  $w$  showed satisfying convergence for time averaging over at least 600 image pairs. The products of two velocity fluctuations, like  $\overline{u'w'}$ , converged slower than mean velocity components and a number of image pairs close to 1000 was required for the convergence to be acceptable, a condition fulfilled in all the results presented here.

The velocity was measured in different vertical planes across the flume width as well as in horizontal planes at different distances above the bottom of the flume. When spatially averaged in the longitudinal direction  $x$ , vertical profiles of  $\langle \overline{u} \rangle_x$  measured in different planes exhibited a very slight asymmetry around the middle plane due to some randomness in the placement of shells at the bottom of the flow. Nevertheless, measurements in vertical planes located at  $y = -5.0$ ,  $y = -2.5$ ,  $y = 0.0$  (middle plane),  $y = +2.5$  and  $y = +5.0$  cm were averaged to obtain profiles of  $U(z) = \langle \overline{u}(x, y, z) \rangle_{xy}$ .

The friction velocity  $u^*$  was estimated using the vertical profiles of the mean spatially averaged vertical component of the turbulent stress tensor  $\langle \overline{u'w'}(x, y, z) \rangle_{xy}$ . For a flow in an infinitely large flume, the turbulent stress tensor profile would be linear above the rough elements (shells), decreasing towards

zero at the free surface. This linear behavior was observed for the high density C configuration, but the zero value was reached well before the free surface, because of the boundary layers developed along the lateral walls of the flume that limit the growth of the bottom boundary layer. In the lower density cases A and B, the secondary circulation driven by anisotropy of the turbulence was strong enough to yield non-linear vertical profiles of  $\langle \overline{u'w'}(x, y, z) \rangle_{xy}$ . In all cases, the value of  $\langle \overline{u'w'}(x, y, z) \rangle_{xy}$  was maximal near the shell crest. We tested many ways of extracting the friction velocity from these curves and found a better agreement with previous studies when the friction velocity was chosen as the maximal value of the square root of  $\langle \overline{u'w'}(x, y, z) \rangle_{xy}$ , corresponding roughly to the average value in the rough and inertial sublayers chosen by Cheng and Castro (2002). For each experimental design, roughness ( $z_0$ ) and displacement ( $d$ ) lengths were estimated by fitting a log-law on the upper mean velocity profiles. The exponential decay parameter  $a$  was obtained by fitting the data between  $z = 0$  and  $z = 3.2$  cm.

Bed shear stresses  $\overline{u'w'}$  and  $\overline{v'w'}$  were estimated from velocity measurements in a horizontal plane at  $z = 1$  cm above the bottom. Since measurements in horizontal planes only provide values for the horizontal velocity components,  $u$  and  $v$ , to estimate the vertical velocity component,  $w$ , we integrated the continuity equation  $\partial u/\partial x + \partial v/\partial y + \partial w/\partial z = 0$  with a no slip condition at the bottom and a linear distribution for the vertical profiles of  $u$  and  $v$  between the bottom and the measurement plane. This crude estimation is based on the assumption that the fluctuations of  $w$  are driven by coherent structures with typical length scales larger than the 1 cm depth layer between the bottom and the measurement plane. Converged values of  $\overline{u'w'}$  and  $\overline{v'w'}$  were then calculated. On the intersection lines of the  $z = 1$  cm horizontal plane with different vertical planes  $y = -5.0$ ,  $y = -2.5$ ,  $y = 0.0$  (middle plane),  $y = +2.5$  and  $y = +5.0$  cm, an agreement for the  $\overline{u'w'}$  profiles was checked that supports this approach.

## 2.4 Numerical simulations

To gain a further understanding of the impact of slipper limpets on the transport properties of the turbulent boundary layer, two-dimensional numerical simulations of the flow near limpet-like obstacles were performed for various densities of chains and three flow conditions. Results from two-dimensional simulations certainly differ in detail from the

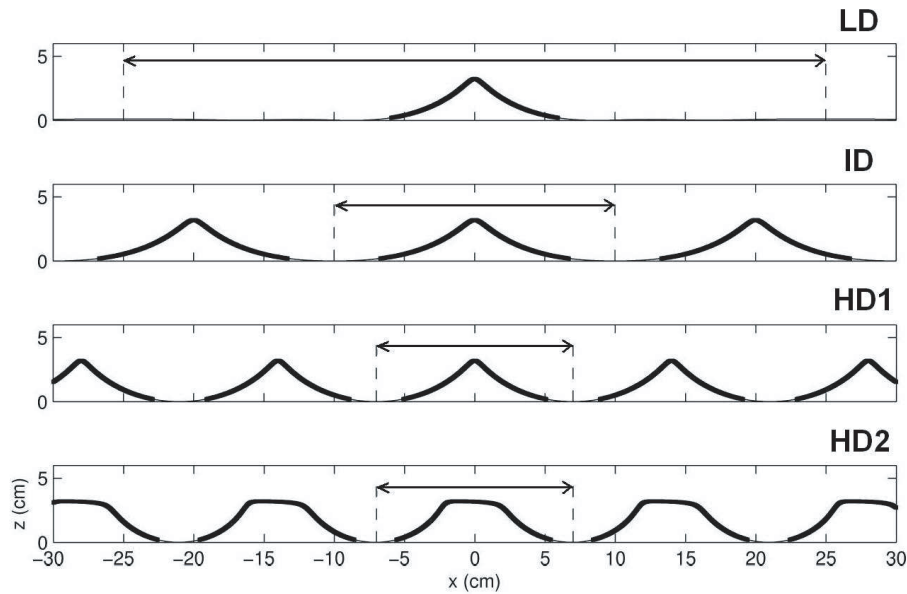


**Fig. 4.** Bedforms used in the numerical simulations: low (LD), intermediate (ID) and high (HD1 and HD2) densities of shells. The horizontal arrow indicates the spatial period of the bottom boundary. Thick lines indicate solid boundaries, with zero-flux conditions in the numerical simulations. Thin lines (below  $z = 0.2$  cm) correspond to a mobile sediment bed.  $x$  is the horizontal coordinate in the flow direction and  $z$  the vertical coordinate.

three-dimensional flow in the nature or in the laboratory experiment. Nevertheless, these simplified two-dimensional simulations are a paradigm of the boundary layer above large roughnesses (with flow separation downstream) and therefore are expected to show similar trends as in three-dimensional flows with respect to the roughness density parameter.

The 2DHV model (Guizien 2005) solves the Reynolds-averaged equations over a 2D topography relying on the transitional  $k-\omega$  turbulent closure proposed by Guizien et al. (2003). The equations are formulated for the potential and vorticity functions and the new system of equations is solved numerically on an orthogonal, curvilinear grid based on the conformal mapping function with the following boundary conditions applied. At the bottom, we prescribe the turbulent kinetic energy  $k$  and velocity potential equal zero, meanwhile the value of  $\omega$  is fixed depending on whether a smooth or rough wall should be modeled (Saffman 1970). At the top of the boundary layer, we forced the outer flow and the vanishing of turbulence at 42 cm above the bed. When necessary, a water depth of 80 cm was also tested. Three values for the outer steady current  $U_\infty$  were tested ( $16 \text{ cm s}^{-1}$ ,  $39 \text{ cm s}^{-1}$  and  $55 \text{ cm s}^{-1}$ ). The conformal mapping function set limitations on the roughness shape. Hence, the form of the shells could be only approximatively reproduced in the simulations. We tested two shell shapes (Fig. 4c, HD1 and 4d, HD2) corresponding to  $H = 3.2$  cm high slipper limpet chains with a density of one chain every 14 cm (high density case). For the sharpest shape (Fig. 4c), two lower densities were also tested with one chain every 20 cm (intermediate density case, Fig. 4b, ID), and one chain every 50 cm (low density case, Fig. 4a, LD). Finally, discretized equations were solved using an Alternate Direction Implicit scheme on an exponential mesh along the vertical

axis (109 points) and a regular mesh along the horizontal axis (101 points).

Sediment suspension was computed by solving the transport equation for the concentration  $c$  in an analogous way to those describing the hydrodynamics. Based on the field data, the bed sediment in the area consists of muddy sand (with a low percentage of the fraction below  $63 \mu\text{m}$ ). Hence, we performed the numerical simulations for a bed sediment with a non-cohesive behaviour and a median diameter  $d_{50} = 350 \mu\text{m}$  (grain roughness is  $k_N = 0.07 \text{ cm}$ ). The suspended concentration was computed for a sand fraction ( $d_1 = 200 \mu\text{m}$  with settling velocity  $w_{s1} = 2.5 \text{ cm s}^{-1}$ ) and a fine-grained fraction ( $d_2 = 63 \mu\text{m}$  with settling velocity  $w_{s2} = 0.37 \text{ cm s}^{-1}$ ). At the bottom boundary, the concentration at two median grain diameters above the bed is taken as the largest of  $c_a$  and  $c_b$ , where  $c_a$  is the concentration resulting from erosion and  $c_b$  is the concentration at the same height assuming zero flux perpendicular to the ripple surface (resulting from deposit). The bed can only be eroded between shells, that is the area defined by  $z$  ranging between 0 and 0.2 mm (Fig. 4). In these areas,  $c_a$  is the reference concentration defined by Engelund and Fredse (1976) formula. Along the shells surface,  $c_a$  was set to zero. At the top of the model domain, a vertical zero-flux condition was applied.

Adopting the same approach as for the laboratory experiments, the hydrodynamical parameters were estimated. The friction velocity  $u^*$  was chosen as equal to the maximal value of  $\langle \overline{u'w'} \rangle_x$ . Then, values of the roughness length  $z_o$  and of the displacement length  $d$  were calculated by fitting the mean velocity profile with a log-profile for  $z$  ranging between 3.2 cm ( $6 z_o$ ) and 10 cm ( $0.2$  to  $0.3 D$ , where  $D$  is the water depth) defined by Cheng and Castro (2002) for the low (LD),

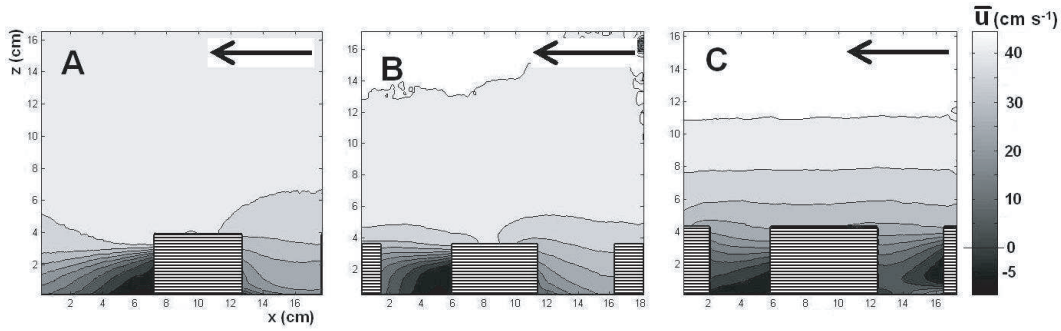


**Fig. 5.** Magnitude of the longitudinal velocities  $\bar{u}$  of a flow over a bed of shells in A, B, C configurations. Measurements are made in the middle plane  $y = 0$  of the flume. The main flow is in the longitudinal direction and goes from the right to the left in the figures, as indicated by the arrows. The horizontal stripes indicate area hidden by the shells, where measurements are not available.  $x$  is the horizontal coordinate in the flow direction, parallel to the bottom of the tank, and  $z$  the vertical coordinate, perpendicular to the bottom of the tank.

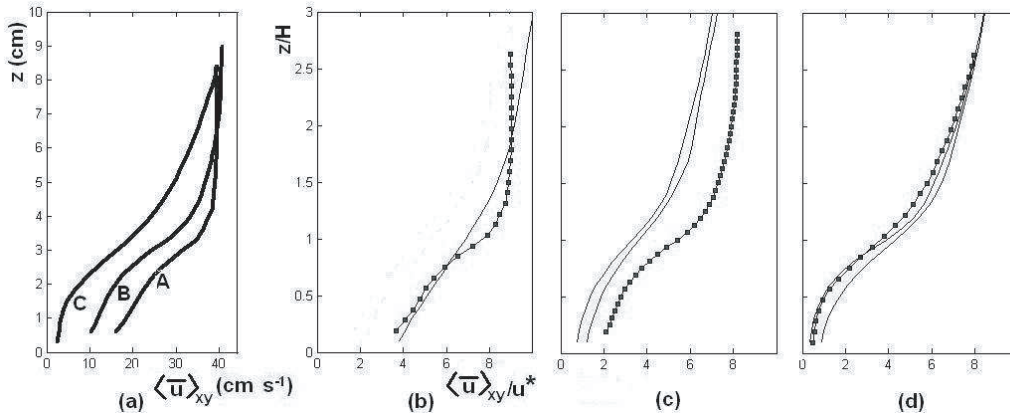


**Fig. 6.** Vertical profiles of the mean spatially averaged longitudinal velocity  $\langle \bar{u} \rangle_{xy}$ . (a) Measured profiles for the three different distributions of shells. Measured profiles normalized with  $u^*$  for the three A, B and C configurations are plotted with symbols, respectively in (b), (c) and (d), along with the profiles (thin lines) obtained by McDonald (2000) for comparison (with values of  $\lambda_f$  and configuration (square or staggered) given in Table 2).

intermediate (ID) and one high density cases (HD2). For the high density case HD1 with  $D = 42$  cm, the value for  $z_0$  restricts the log zone to  $9 < z < 13$  cm by moving upward the lower limit. To gain sensitivity, a computation with  $D = 80$  cm was performed which enabled to extend the log fit zone to  $9 < z < 24$  cm. The values for  $z_0$  and  $d$  agreed in the computations for the two water depths but we considered that the values obtained for the larger water depth were more precise. The exponential decay  $a$  in the canopy region was obtained by fitting the data in the region  $0 < z < 3.2$  cm.

### 3 Results

#### 3.1 Hydrodynamic properties in the laboratory experiments

Typical horizontal mean velocities  $\bar{u}$  in the middle plane are shown in Figs. 5a-c for the three different configurations. The striped areas are regions where no velocity could be measured because of the presence of shells. Some general features

can be derived from these pictures. First, the mean flow is decelerated by the obstacles: the velocity in the canopy layer decreases with the frontal density of the rough elements. Behind individual shells,  $\bar{u}$  exhibits negative values that delimitate recirculation regions. The longitudinal extension of these regions is roughly equal to the height of the obstacles. The presence of these recirculation regions is also highlighted by the distribution of vertical velocity. Downward motions decrease as the frontal density of rough elements increases. It should be kept in mind that the flow in the canopy layer CL is fully three-dimensional, as illustrated indirectly by horizontal distribution of benthic shear stress (Fig. 7).

Profiles of  $U(z) = \langle \bar{u}(x, y, z) \rangle_{xy}$  for the three configurations are drawn in Fig. 6a. For different shell densities the velocity  $U$  increases with height until a constant value  $U_\infty = 40$  cm s<sup>-1</sup> is reached. This is in agreement with the finite thickness of the bottom boundary layer also apparent in the vertical profiles of  $\langle u'w' \rangle_{xy}$  discussed above (data not shown). The height at which the velocity becomes constant increases with the frontal density of shells, in accordance with what was observed in the profiles of  $\langle u'w' \rangle_{xy}$ .

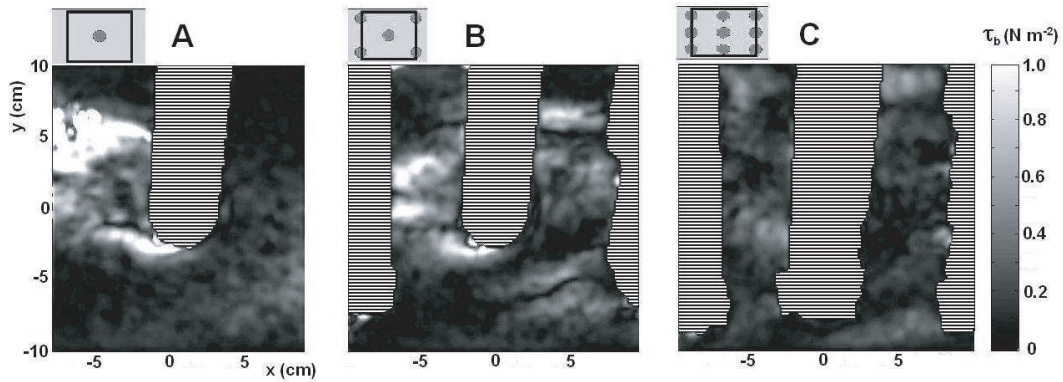


**Fig. 7.** Greymaps representing the distribution in the horizontal plane  $z = 1$  cm of the estimated benthic shear stress  $\tau_{bed}$  [ $\text{N}/\text{m}^2$ ] of the flow for the three A, B and C configurations. The horizontal stripes indicate areas hidden by the shells, where measurements are not available.

**Table 2.** Overview of experimental (left column) and theoretical values of the characteristic non-dimensional parameters that govern a turbulent flow above a rough surface. The theoretical values originate from McDonald (2000) and were obtained for regular cube patterns.

	Shell configurations	Values of McDonald (2000) for square (sq) or staggered (st) cube patterns	
	A		
$\lambda_f$	0.05	0.05 (sq)	
$a$	0.88	0.63	
$z_0/H$	0.0266	0.0048	
$d/H$	0.38	0.066	
$u^*/U_\infty$	0.106		
$\tau_b/\tau_H$	0.149		
	B		
$\lambda_f$	0.12	0.11 (st)	0.16 (st)
$a$	1.14	1.20	1.64
$z_0/H$	0.043	0.14	0.15
$d/H$	0.59	0.26	0.32
$u^*/U_\infty$	0.121		
$\tau_b/\tau_H$	0.106		
	C		
$\lambda_f$	0.24	0.20 (sq)	0.33 (sq)
$a$	2.37	1.80	2.78
$z_0/H$	0.083	0.080	0.077
$d/H$	0.63	0.42	0.57
$u^*/U_\infty$	0.124		
$\tau_b/\tau_H$	0.077		

Values for  $u^*/U_\infty$  are given in Table 2 for the experiments with configurations A, B and C. Figs. 6b-d show the vertical profiles of non-dimensional longitudinal velocities  $U(z)/u^*$  and compare them to the profiles of McDonald (2000) obtained for regular arrays of cubic elements for roughly the same frontal density  $\lambda_f$ . Values of the relevant parameters that describe these vertical profiles ( $d$ ,  $z_0$  and  $a$ ) are given in Table 2 for the three experiments. Values obtained by McDonald (2000) for similar frontal densities, used to plot the theoretical curves in Figs. 6b-d, are reported for comparison.

The canopy  $U_c$ , the reference  $U_{ref}$  and the exchange  $U_E$  velocity were computed for the turbulent boundary layer flow above the three different shell configurations in our experiments (Table 3). Predictions by Bentham and Britter (2003) for different frontal densities are also reported. Experimental

values for the flow above shells decreases with  $\lambda_f$  for the three tested configurations.

From the horizontal maps of the shear stress tensor components  $\overline{u'w'}$  and  $\overline{v'w'}$  (see horizontal maps in Figs. 7a-c at the bottom, horizontally averaged values of the bed friction were calculated for the three different configurations. The ratios of the bottom to shell crest averaged shear stresses values  $\tau_b/\tau_H$  are given in Table 2. This ratio decreases as the frontal density of shells increases.

### 3.2 Hydrodynamic properties from the 2D numerical simulations

Figure 8 shows vertical profiles obtained for the mean x-averaged longitudinal velocity  $U(z) = \langle \bar{u} \rangle_x$ . Curves for

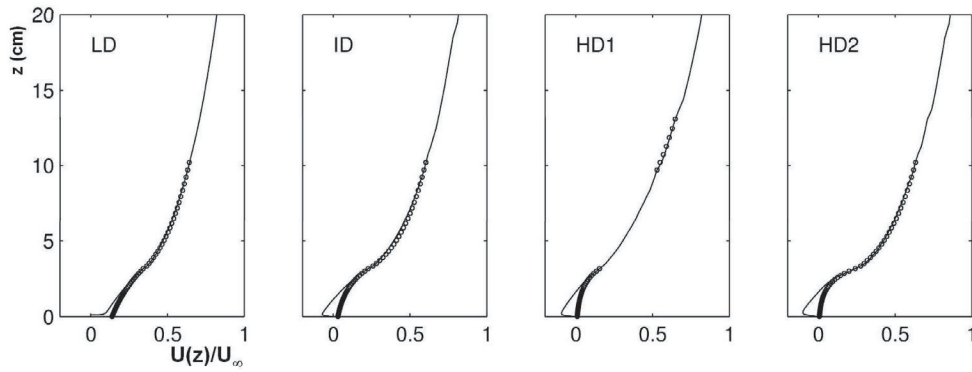


**Fig. 8.** Vertical profiles of the mean  $x$ -averaged longitudinal velocity  $\langle \bar{u} \rangle_x / U_\infty$  computed with the 2D numerical model for the LD (low density), ID (intermediate density), HD1 (high density) and HD2 cases. Fits for the log law and for the canopy exponential decay are represented by hollow circles.

**Table 3.** Values for the exchange velocity  $u_E$  and the in-canopy characteristic velocity  $u_C$  given by Bentham and Britter (2003), Hamlyn and Britter (2005), and computed from our experimental data for the three configurations.

	Bentham & Britter (2003)				Hamlyn & Britter (2005)			shells A	shells B	shells C
$\lambda_f$	0.05	0.1	0.15	0.25	0.0625	0.16	0.44	0.05	0.12	0.24
$u_C/u_*$	5.1	4.0	3.8	2.8	5.34	4.56	2.08	5.4	3.5	1.9
$u_{ref}/u_*$	8.6	7.3	6.9	6.9	12.35	12.22	11.76	9.3	8.3	7.9
$u_E/u_*$	0.29	0.31	0.32	0.25	0.135	0.115	0.038	0.26	0.21	0.17
$u_E/u_{ref}$	0.033	0.042	0.047	0.036	0.011	0.0094	0.0032	0.028	0.025	0.021

**Table 4.** Overview of pertinent non-dimensional parameters that govern a turbulent flow above 2D transverse obstacles, inferred from the numerical simulations. LD: low density of shells, ID: intermediate density, HD: high density. For the two high density cases, computations were performed for two water depths ( $D = 42$  cm and 80 cm).

Shell density	$D$ (cm)	$\lambda_{f2D}$	$u^*/U_\infty$	$d/H$	$z_o/H$	$a$	$\tau_b/\rho u_*^2$	$\tau_b/\tau_H$
LD	42	0.064	0.078	0.354	0.103	0.9	0.111	0.113
ID	42	0.160	0.081	0.587	0.126	2.0	0.043	0.050
HD1	80	0.229	0.121	1.08	0.410	2.8	0.023	0.055
HD2	42	0.229	0.091	0.508	0.154	3.5	0.034	0.103

**Table 5.** Values for the exchange velocity  $u_E$  and the in-canopy characteristic velocity  $u_C$  computed from the 2D numerical simulations.

	$\lambda_{f2D}$	$u_E/u^*$	$u_C/u^*$	$u_{ref}/u^*$	$u_E/u_{ref}$
LD	0.064	0.23	3.04	7.44	0.031
ID	0.160	0.20	1.54	6.60	0.030
HD1	0.229	0.32	0.72	3.80	0.086
HD2	0.229	0.21	1.36	6.13	0.034

the three external velocity  $U_\infty$  values tested collapsed when scaled with  $U_\infty$ . Values for  $z_o/H$ ,  $d/H$  and  $a$  are given in Table 4 for different values of the 2D frontal density defined as  $\lambda_{f2D} = H/L$  where  $L$  is the spatial period of the bottom pattern. The piecewise fits for the canopy and inertial sublayer mean velocity profile are plotted above the simulated ones in Fig. 8. The canopy  $U_C$ , the reference  $U_{ref}$  and the exchange  $U_E$  velocity were computed for the four numerical test cases (Table 5).

To estimate the drag at the bottom that drives solid matter transport, averaged values of  $\overline{u'w'}$  in regions with  $z < 0.1$  cm were extracted from the numerical simulations. When divided by the friction velocity  $u^*$ , the calculated ratios indicate how much of the total drag contributes to particle transport. Values of these ratios decrease when the frontal density of obstacles increases (Table 4). Figure 9 shows the evolution of the shear stress along the rough elements for two different grain sizes and the different frontal densities. In the erodible area (between shells), the maximum value of the shear stress decreases as the frontal density increases.

Considering these maximal values of the shear stress maxima, only the fine-grain fraction is likely to be eroded. Indeed, computations confirm this expectation: they show that suspended sediment concentrations for the sand fraction ( $d_2 = 200 \mu\text{m}$ ) are negligible (data not shown) and that the fine-grained fraction ( $d_1 = 63 \mu\text{m}$ ) is largely eroded. However, unexpectedly, suspended sediment concentration levels increase as the frontal density of shells  $\lambda_f$  increases (Fig. 10).

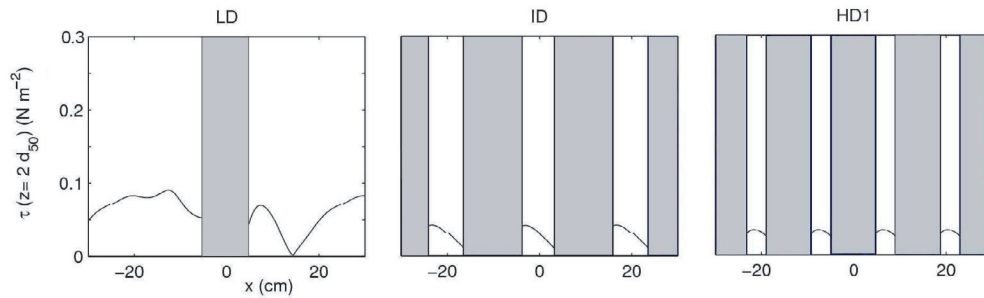


**Fig. 9.** Along bed roughness variations of the bed shear stress  $\tau$  computed with the 2D numerical model for the LD, ID and HD1 cases. Shaded area indicates solid boundaries with zero-flux conditions that represent the shells.

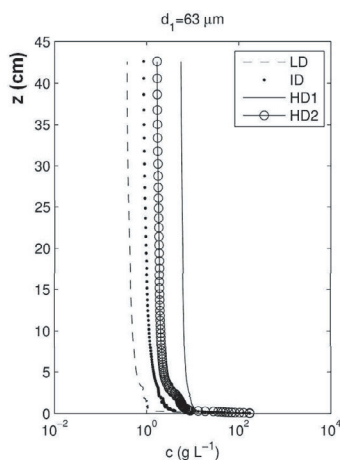


**Fig. 10.** Vertical profiles of suspended sediment concentration  $c$  for a fine-grained fraction ( $d_1 = 63 \mu\text{m}$ ) computed with the 2D numerical model for the LD, ID, HD1 and HD2 cases. It was assumed that this fraction represents 10% of the bed granulometry (a sediment bed with a median diameter  $d_{50} = 350 \mu\text{m}$ ).  $z$  is the vertical coordinate.

### 3.3 Field measurements of near-bottom current and suspended sediment concentration

Tide-related particle distribution showed maximal SPM (for total suspended particulate matter), POM (for particulate organic matter) and PIM (for particulate inorganic matter) concentrations near bottom during slack tide (especially around high tide; e.g. in Fig. 11) in the two study sites, except for neap tide conditions (no clear trend in this case). Thus, the data would reflect particle sedimentation when the current velocity is weak and particle dilution on the vertical when increasing flow velocity induces increasing turbulent mixing in the water column. The two study sites exhibited different patterns in the tide-related evolution of organic matter percent in SPM. The latter was maximum at mid tide near bottom (between 20 and 60–80 cm above the bottom) in S1 (with minimum values at slack tide near bottom), while maximum values near bottom were recorded around slack tide in S2. At mid tide, opposite trends were found on the vertical in S2 with organic matter percent increasing with the distance above the seabed.

Mean SPM (total suspended particulate matter) and POM (particulate organic matter) concentrations in the first 2 m above the bottom (values averaged between the 6 sampling depths and the 9 sampling times) exhibited higher values at S2 than at S1 during spring tide, but similar values at neap tide and for intermediate tides (Table 6). Mean SPM and POM concentrations were in the ranges  $5\text{--}13 \text{ mg L}^{-1}$  and  $1\text{--}3 \text{ mg L}^{-1}$ , respectively. Mean percent organic matter in SPM was in the range 16–22% with higher value at S1 during spring tide, but similar values in the two other cases. Mean percent organic matter in the near-bottom sampling bottle (B1; 20 cm off the bottom) was higher in S1, except for neap tide (no significant difference; Table 6). In September 2005, the site with low *Crepidula* densities (S2) exhibited strong variations in mean time-averaged depth-averaged SPM and POM concentrations between spring tide and neap tide (1.75 to 2-fold differences), while differences were in the range 10–17% at the site with high *Crepidula* densities (S1; Table 6). Time-averaged SPM and POM concentrations followed typical Rouse distributions on the vertical in the two study sites with highest variations in particle concentration over a tidal cycle during spring tide and lowest during neap tide. Standard deviations of the mean values were highest at 20 cm off the bottom at S1, while the last two or three bottom levels (between 20 and 60 cm off the bottom) were concerned at S2. The variations in percent organic matter at 20 cm off the bottom were particularly high at S1 on 13 April 2006 (mean  $\pm$  SD:  $25.4 \pm 17.0\%$ ) compared with the five other sampling levels (mean: 18.5–19.8%, SD: 1–6%), highlighting PIM (Particle Inorganic Matter) resuspension mainly limited to the 20 first centimeters off the bottom, and maximal POM concentration near the water-sediment interface. Seasonal variations of percent organic matter in suspended particles were more pronounced at S2 (from 15–17% on 20 September 05 to 20–23% on 15 April 06) than at S1 (from 18–21% on 21 September 05 to 19–25% on 13 April 06).

For the surveys of April 2006, measurements of the horizontal and friction velocities at 40 cm above the bottom (Fig. 12) show that near-bottom currents are non-symmetric, with eastward (flood) currents stronger than westward (ebb) currents, in accordance with a slow drift of water towards the estuary. Dividing the current velocity by the friction velocity, crude estimations of the roughness length  $z_0$  can be inferred from these measurements: on average, values of the roughness length are larger at site S1 than at site S2.

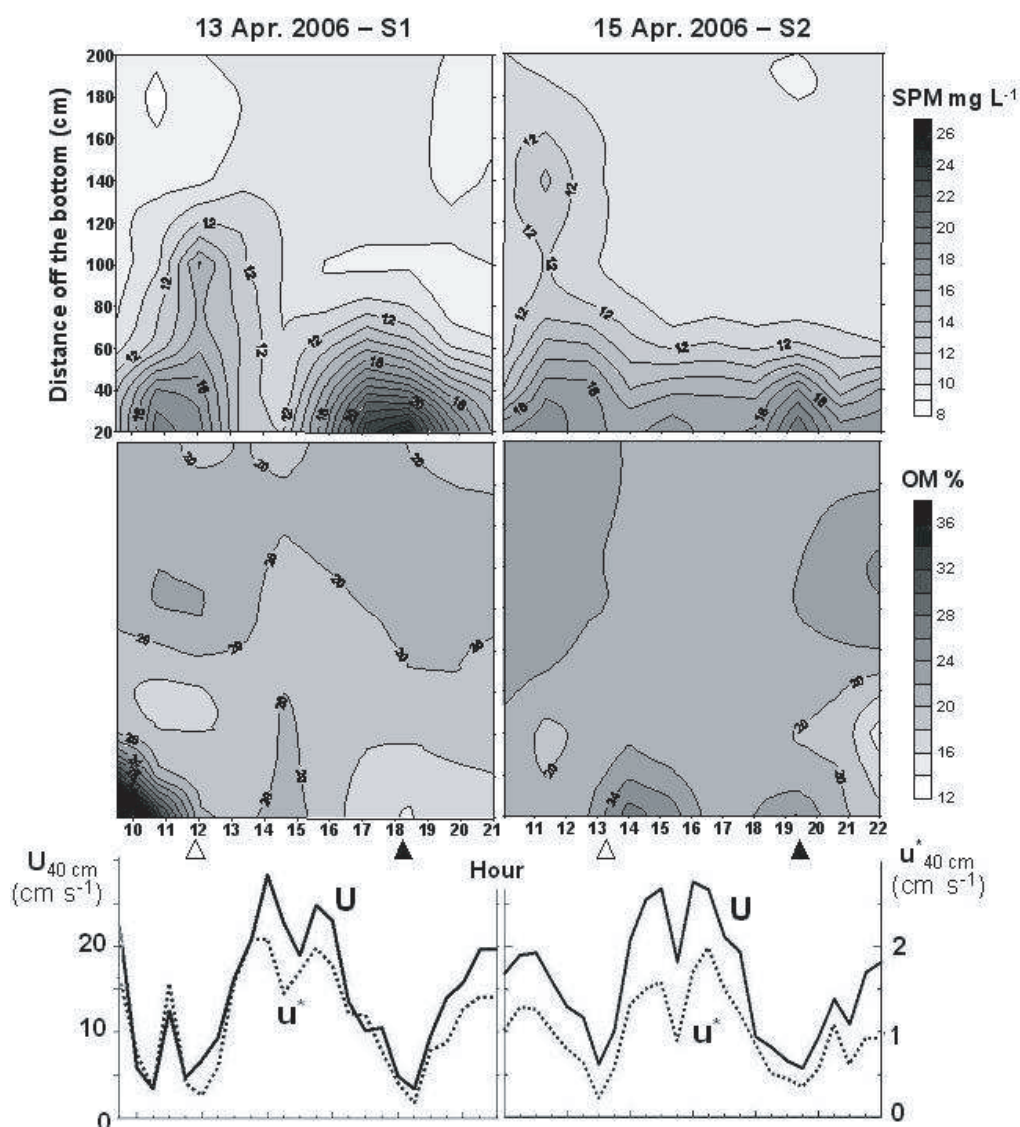


**Fig. 11.** Tide-related distribution of total suspended particulate matter concentrations (SPM) and percent particle organic matter concentrations (OM%) measured between 20 cm and 2 m off the bottom in the Bay of Brest in April 2006 (at both sites S1, S2). Open triangles: low tide; plain triangles: high tide. Kriging interpolation was performed using SURFER<sup>®</sup>. Current (U) and friction velocities ( $u^*$ ) measured at 40 cm above the bottom at the same positions are plotted in the lower part of the figure.

**Table 6.** Mean (SD,  $\text{mg L}^{-1}$ ) total suspended particulate matter (SPM) and particulate organic matter (POM) concentrations, and mean (SD) percent organic matter in SPM measured in the Bay of Brest in September 2005 and April 2006. Water samples were collected every 90 min on 12 h periods at 20, 40, 60, 100, 140 and 200 cm off the bottom with a bottom-landing water sampling system (see Bale and Barrett 1995 for technical information on the sampling system). Values were averaged on time and depth. Time-averaged mean percent organic matter in SPM at 20 cm off the bottom (B1) is also reported. See the methodology section for geographical coordinates of the two study sites. See <http://marees.free.fr/coefficients.html> for the definition of the tidal coefficients. Spring tides: values > 90; neap tides: values < 50.

Site	Date	Tidal coefficients	SPM ( $\text{mg L}^{-1}$ )	POM ( $\text{mg L}^{-1}$ )	Organic matter (%)	Organic matter in B1 (%)
S1	21 Sept. 2005	100–94	5.58 (1.71)	1.05 (0.22)	19.6(0.9)	18.2(2.6)
S2	20 Sept. 2005	109–106	12.53 (2.85)	1.96 (0.42)	15.8(0.7)	15.6(1.1)
S1	24 Sept. 2005	52–44	5.07 (1.33)	0.9 (0.18)	18.1(1.2)	16.8(3.3)
S2	23 Sept. 2005	70–61	6.1 (1.91)	1.12 (0.22)	19.2(1.4)	17.4(3.8)
S1	13 April 2006	84–86	12.66 (3.39)	2.55 (0.89)	20.3(2.5)	25.4(17.0)
S2	15 April 2006	88–87	12.68 (3.02)	2.74 (0.72)	21.6(1.2)	22.6(5.5)

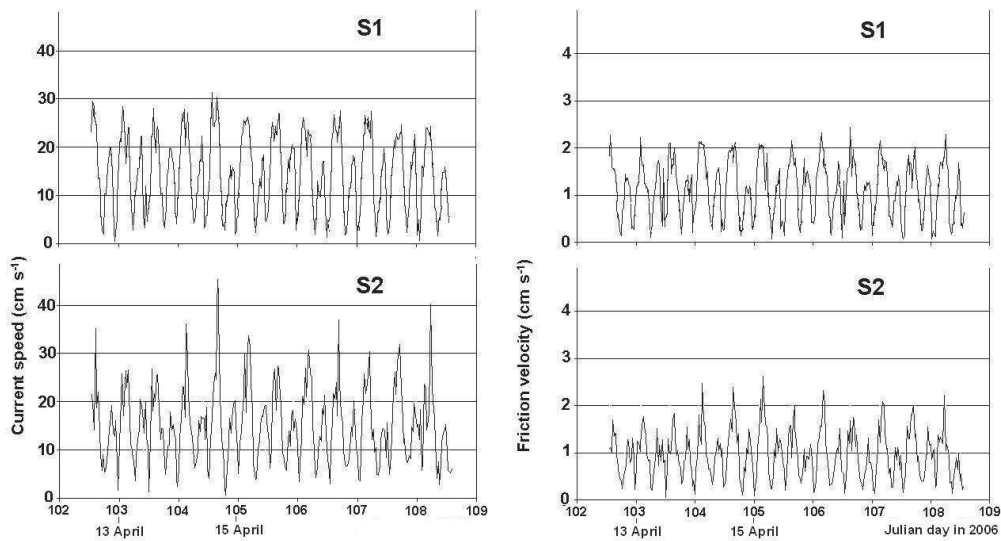


**Fig. 12.** Current and friction velocities measured at 40 cm above the bottom in the Bay of Brest in April 2006 at the two sites S1 and S2. See text and Table 6 for the method and the tidal conditions during the experiments.

## 4 Discussion

### 4.1 Mean velocity vertical profile

A very good agreement is found between the mean velocity profile obtained in our experiment and that of McDonald (2000) for the highest density (Fig. 6d). For the intermediate density (Fig. 6c), the profiles are very similar in shape, and the discrepancy is probably due to the uncertainty in the value of  $u^*$ . For the low density (Fig. 6b), the boundary layers developed along the lateral walls become predominant in the upper part of the profile, where the velocity is almost constant, and precluded any comparison in this part of the flow. For the lowest part of the rough sublayer i.e.  $z < H$ , the exponential behavior of the experimental profiles inside the canopy layer, measured by the attenuation coefficient  $a$  defined in McDonald (2000), is in very good agreement with results obtained for regular arrays of cubic elements. The parameters  $d$  and  $z_0$  of formula (2) have been extracted from the upper part ( $z > H$ ) of the experimental profiles of Fig. 6. Not surprisingly, we found a very good agreement with results of McDonald (2000) for the higher density, while different values were obtained for the other two densities. For the lowest density, this discrepancy is likely to be due to the uncertainty in the determination of  $u^*$  and the effect of side walls. However, for the intermediate density, the shape of the shells, smoother than the cubes used by McDonald (2000), could also explain this difference (see Bentham and Britter 2003).

Like in the flume experiments, the canopy layer velocity in the 2D numerical simulations is stronger decelerated as the density is higher. Moreover, the increase of the roughness parameter  $z_0$  with the frontal density  $\lambda_{f2D}$  reproduces well the trend observed in the experiments. Yet, values for  $z_0/H$  are larger in the 2D numerical simulations than for the 3D experiments for the same value of frontal density, but these results are in agreement with experimental results by Fredse et al. (1999)

over 2D ripples ( $z_0/H = 0.08$  for  $\lambda_{f2D} = 0.159$ ) and recent numerical studies on artificial obstacles (Orlandi et al. 2006). Our values for  $z_0/H$  are also consistent with values reported in the literature over densely packed 3D roughnesses, between 0.066 to 0.13 (Kamphuis 1974; Bayazit 1976), except for the high density case, especially over the sharp shape which exhibited a value of 0.41. The increase of the simulated roughness values in comparison with the experimental data is due to the strong blocking effect associated with 2D obstacles that does not exist for 3D rough elements. In Figs. 8b, c and d, a reverse flow clearly forms near bottom, associated with a vortex trapped between two successive obstacles. Such blocking also occurs in 3D arrays, but is limited to small regions near individual obstacles. As a consequence of this blocking effect, the exponential model proposed by McDonald (2000) in the canopy layer does not apply for the intermediate and high densities. Meanwhile, a good fit is still obtained for the low density where the blocking is not observed, with a corresponding attenuation coefficient  $a$  very close to the one obtained in the experiments for a similar frontal density.

In the numerical simulations, the roughness shape effect was tested for the high density. The value of the hydraulic roughness was different for the two different shapes. As noted by Bentham and Britter (2003), this difference is related to the drag coefficient of each individual shape. Assuming a simple relationship of the form  $z_0/H = C\lambda_f$ , the drag coefficient lied between 0.35 and 0.5 in the experiments with 3D obstacles. These values are lower than 1, the value inferred for the cubic or rectangular obstacles in urban canopies.

As far as the displacement length  $d$  is concerned, the 2D simulations values for the low and intermediate densities are very similar to the one obtained in the flume experiments. Values for  $d/H$  in the 2D simulations for the intermediate and high densities lay in the range of values reported in the literature over densely packed 3D spherical rugosities, i.e. between 0.65 to 0.85 (Bayazit 1976). Moreover, the increase of

the displacement length  $d$  with the frontal density is in agreement with trends observed in previous studies. Finally, the 2D simulations illustrate how the displacement length is sensitive to the roughness shape: different values are found for  $d$  even for a same value of the frontal density of obstacles.

#### 4.2 Exchange between the canopy layer and the free stream

According to Bentham and Britter (2003), sparse canopies do not generate much turbulence, hence  $U_E/U_{ref}$  should be rather small. Increasing obstacle density enhances the mechanical production of turbulence, resulting in increasing exchange. The value of  $U_E/U_{ref}$  then increases with packing density up to the point where skimming flow sets in and the in-canopy and above-canopy flows are decoupled, leading to a reduction of the exchange. By contrast, in the flume experiments,  $U_E/U_{ref}$  decreased as  $\lambda_f$  increased, for low values of  $\lambda_f$ . In addition, for the shells B and C configurations, our  $U_E/U_{ref}$  experimental values were about half the ones obtained by Bentham and Britter (2003) for similar frontal densities. In the numerical simulations,  $U_E/U_{ref}$  ratios also decreased as  $\lambda_f$  increased for the two lowest densities. The same trend was observed in LES numerical simulations by Hamlyn and Britter (2005), where  $U_E/U_{ref}$  values were even lower than in our experiments: the authors suggested that the way McDonald (2000) inferred the friction velocity  $u^*$  from the velocity profiles overestimated the real value. Indeed, our determination of  $u^*$ , based upon profiles of  $\overline{u'w'}$ , is a better estimation and gives credit to the view of Hamlyn and Britter (2005). In Hamlyn and Britter (2005), due to limitations of the numerical simulations, the pressure field was used to calculate the canopy velocity  $U_C$  instead of a quadratic averaging procedure. These changes in the definition of the canopy velocity  $U_C$  and in the shape of the roughness could explain the difference in exchange velocity values.

In the 2D numerical simulations,  $U_E/U_{ref}$  is significantly higher for the highest density with the sharp shape (HD1). When the roughness shape is more cubic (HD2),  $U_E/U_{ref}$  ratio is lower, closer to the one obtained by Bentham and Britter (2003) than to the one observed in our laboratory experiments. This point highlights the importance of the roughness shape, which was already emphasized for the roughness and displacement lengths. The lower values for the exchange velocity inferred from our experimental results on rounded shells may be attributed to the shape, since cubes were used in Bentham and Britter (2003). The numerical simulations further suggest that sharpest shapes (HD1) would enhance the exchange between the canopy layer and the free stream. This might result from the vertical position of the vortex generated by the obstacle.

Finally, a simple model with a constant velocity throughout the canopy layer as proposed by Bentham and Britter (2003) appears inappropriate to describe the strong reverse flow obtained in the numerical simulations over 2D obstacles. This reverse flow that results from the blocking of the vortex behind the obstacles may also appear for higher densities of 3D obstacles, thus limiting the application range of the simple theory by Bentham and Britter (2003) to sparse canopies.

#### 4.3 Bed shear stress and sediment erosion around large roughnesses

In the flume experiments, a clear sheltering effect by the rough elements is shown, with  $\tau_b/\tau_H$  ratios beneath 0.15 even for the relatively low density configuration. Beside, this sheltering effect becomes more important as the frontal density increases. A similar trend is obtained in the 2D numerical simulations with even lower  $\tau_b/\tau_H$  values for the same frontal densities. It should be stressed that this sheltering effects is also amplified by the decrease in the area available for the solid matter as the packing density increases.

Other interesting features appear when one looks at the horizontal maps plotted in Figs. 7a-c. The repartition is strongly inhomogenous in the low density and intermediate density cases, with regions of high shear stress behind individual rough elements. This means that even in cases where the horizontally-averaged bottom shear stress does not seem strong enough to induce particulate matter transport, some regions behind individual elements experience shear stress values high enough to generate a flux of solid matter into the canopy flow. As the density increases, the distribution becomes gradually more homogenous, and the difference between different zones fades. The same features also appears in the 2D numerical simulations, with localized area of high stress when the density is low (Fig. 9a). Since solid particles on a horizontal plane are put in movement as soon as the shear stress exceeds a critical value that depends on the size and density of the particles, these results suggest that bed erosion should decrease when the density of shells increases.

Nevertheless, in the 2D numerical simulations, the suspended sediment concentrations increased when the density of the spatial distribution of shells increased (Fig. 10). This is explained by the fact that around large roughnesses, erosion does not only result from turbulent diffusive processes (that drive bottom shear stresses) but also from convective processes (vertical velocity). These latter processes become relatively more important as the obstacles get closer. Indeed, near-bed upward vertical velocities (up to  $1 \text{ cm s}^{-1}$ ) are observed (data not shown) between the obstacles for either the low or the high frontal density cases. These upward velocities are higher than the fine-grained sediment settling velocity ( $0.37 \text{ cm s}^{-1}$ ) and thus, can lift this sediment size fraction into suspension. These velocities are associated with recirculation regions behind each individual obstacle. Hence, their proportion increases with the density of shells and explains the trend observed for simulated suspended sediment concentrations. However, these 2D simulations may be partly biased compared to 3D cases, since the proportion of the planar surface controlled by the near-bed upward flow is smaller in 3D than in 2D. Therefore, it is likely that in 3D, erosion first decreases when the density of roughnesses increases (due to the decrease in bed shear stress intensity), but then increases (due to near-bed upward velocities) when the density further increases.

#### 4.4 Confrontation with the field survey

In non-cohesive sediments, solid particles on a horizontal plane are put in movement as soon as the bottom shear stress

exceeds a critical value that depends essentially on the size and density of the particles, and in a lesser extent, on their shape. In general, natural sediments exhibit complex behaviour, especially if they possess cohesive properties. However, for muddy sands like those found in the Bay of Brest, non-cohesive behaviours are still expected as long as the content of finest particles (lower than  $63 \mu\text{m}$ ) is below 10%. In this case, the critical value may be deduced, for instance, from the Shields curve (Peterson 1999), and compared to the horizontal maps of shear stress to determine which class of sediment may be eroded at the bottom. According to Peterson (1999), locations with bottom shear stress lower than  $0.001 \text{ Nm}^{-2}$  are subjected to burial and excessive scour occurs in locations with values larger than  $0.1 \text{ Nm}^{-2}$  where fine sands begin to move. Desirable benthic shear stresses for suspension-feeding benthic organisms are found in the range  $0.003\text{--}0.03 \text{ Nm}^{-2}$ , where organic matter is gently resuspended and maintained in an aerobic state.

Maps of the bottom shear stress in the flume experiments (Figs. 7a–c) were obtained for external flows of  $40 \text{ cm s}^{-1}$ , with an equivalent boundary layer thickness  $\delta$  ranging from approximately 7 cm to 12 cm, and a friction velocity from  $u^* = 4.24 \text{ cm s}^{-1}$  to  $u^* = 4.96 \text{ cm s}^{-1}$  for the three configurations. For the low and intermediate densities, an important scour would occur if the bottom of the tank was replaced by a bed of fine sand, but lower values of the friction velocity  $u^*$ , and hence, of the bottom shear stress, are measured for the tidal currents in the Bay of Brest. Yet, the values of the bottom shear stress of Figs. 7a–c, or of the spatially-averaged bottom shear stress, non-dimensionalised by the friction velocity  $u^*$ , are the same in a flume experiment or in a tidal turbulent boundary layer. Field measurements of the current and friction velocities (Fig. 12) for a mild tide are in accordance with the modelling of the flow over rough elements: with a roughness length of 0.26 cm (0.08 cm) inferred from the laboratory experiment C (A), representative of the shell density of sites S1 (S2), and a total friction velocity around  $u^* = 2.2 \text{ cm s}^{-1}$  ( $u^* = 2.0 \text{ cm s}^{-1}$ ) at the tidal peak, the maximal velocity would be theoretically around  $27.0 \text{ cm s}^{-1}$  ( $30.3 \text{ cm s}^{-1}$ ) at site S1 (S2), very close to the measured values. Following Kuo et al. (1996), this would correspond to boundary layers thicknesses larger than 5 meters. For the spatially-averaged bottom shear stress, maximal values of  $\tau_b = 0.037 \text{ Nm}^{-2}$  and  $0.060 \text{ Nm}^{-2}$  are then deduced for sites S1 and S2 from ratios  $\tau_b/\tau_H$  in Table 2. Indeed, higher local values are expected to be reached behind individual shells in the low-density site S2, due to the strong spatial heterogeneity of bottom shear stress (Fig. 7a). During a complete tidal cycle, the free velocity, and hence the bottom shear stress, oscillates in the range prescribed by the values calculated for the two sites. Different sediment size classes are then resuspended at different times during the tidal cycle, with differences between the two sites due to the differences in the amplitude of the bottom shear stress.

Notwithstanding the potential impact of current velocity differences during the flood (see Fig. 12), between-site differences in mean particulate matter concentrations during spring tides would signify higher particle resuspension on the muddy sand bottom with few chains of slipper limpets, compared with the high-density area. Indeed, organic matter content in surface sediments is higher at S1 (9.3% on average; Martin et al.,

accepted) than at S2 (5.6%) and should generate higher POM resuspension. This result suggests a sheltering effect by the *Crepidula* shells increasing with the frontal density of shells. It is consistent with both our experimental and numerical results which showed that both average bed erosion and exchange velocity between the canopy and the outer flow decrease as the roughness density increases. In other words, for similar flow intensity, the lower the density of rough elements the higher the resuspension is (and the export of fine particles with the tidal currents). This trend does not seem to be observed for the mild-tide field data of April 2006, though the maximal value of the spatially-averaged bottom shear stress estimated at S2 ( $0.06 \text{ Nm}^{-2}$ ) should be sufficient to trigger silt resuspension (according to Peterson 1999, silts would begin to scour in the range  $0.03\text{--}0.1 \text{ Nm}^{-2}$ ). However, POM resuspension did occur at mid tide on 15 April 2006 (S2), as shown by Fig. 11. We hypothesize that current velocity may not be sufficient in mild-tide conditions to induce massive particle resuspension at S2 (e.g. strong enough to reverse the POM concentration differences in sediments of the two sites). Such between-site differences would mainly occur during the energetic spring tides (e.g. in September 2005), where the bottom shear stress triggers a larger resuspension at S2 than at S1. As far as *Crepidula fornicata* is concerned, these findings are consistent with the observations of a silting trend in areas exhibiting high slipper limpet density, compared with low-density areas where strong tides are still able to trigger silt resuspension. When considering the SPM organic matter contents (Fig. 11), the mid-tide increases near bottom at S1 would highlight resuspension of *Crepidula* biodeposits limited to bottom water (the first 80 cm above the sediment on 13 April 2006) and the possible role played by the sticky mucus, which coats the feces and pseudofeces, against biodeposit erodability. By contrast, the negative concentration gradient on the vertical at S2 at mid tide, and the increases of SPM organic matter contents near bottom at slack tide, would signify that POM erosion and sedimentation would be only governed by hydrodynamic processes in areas with low densities of slipper limpets. Finally, higher sedimentation rates at slack of the high tide, compared with slack of the low tide (Fig. 11) do agree with higher current velocities and subsequent higher particle resuspension during the flood, compared with the ebb (Fig. 12).

## 5 Conclusion

The laboratory and numerical experiments showed how the presence of *Crepidula* shells changed the structure of the near-bottom flow as their density increases. Whereas the apparent roughness length increases with the density, the bottom shear stress itself is reduced by the presence of the shells. In addition, the exchange between the near-bottom region and the flow also decreases as the shell density increases. The overall resulting effect is a sheltering effect by the *Crepidula* shells. Indeed, the apparent friction velocity felt by the tidal flow does not control directly sediment transport and resuspension. Field measurements also support this trend: lower particulate matter resuspension on high-density areas, compared with low-density zones, could signify lower food availability for

suspension-feeding benthic organisms feeding on resuspended phytoplankton cells or microphytobenthos.

More quantitative comparisons between the field survey and the experimental and numerical experiments would require the knowledge of both the near-bottom (0–10 cm above the sediment) hydrodynamic conditions and the exact nature of the bed of sediments. As discussed above, the fact that the between-site differences appear only during energetic spring tides highlights the problem of the choice of the criterium to predict bed erodability. This erodability has been shown to depend also on the biological activity of the slipper limpets (production of mucus-coated biodeposits that can consolidate the bed) that can enhance the bottom shear stress levels required to trigger sediment erosion.

Near-bottom velocity measurements on the two sites and/or hydrodynamical modelling of the Bay of Brest could be coupled with the results of the laboratory experiments to infer the exact conditions at the sediment-water interface. This approach is now in progress. Sediment samples will be collected at the two sites and analysed, to provide a relevant granulometry for a simplified 1D vertical modelling of the sediment resuspension during a tidal cycle. Finally, in locations where the shell density is still low, other living species, mainly macroalgae Rhodophyceae, may contribute to the hydrodynamic properties of the benthic boundary layer. The former should be taken into account in the modelling of bottom shear stress and exchange velocity.

*Acknowledgements.* The authors gratefully acknowledge financial support from the Programme National en Environnement Côtier (PNEC) (nationwide French programme for the coastal environment). This work is a contribution within an innovative and transversal action entitled “érodabilité des sédiments naturels” (erodability of natural sediments).

## References

- Bale A.J., Barrett C.D., 1995, A bottom-landing water sampling system for the benthic boundary layer. *Neth. J. Sea Res.* 34, 259-266.
- Bayazit M., 1976, Free surface flow in a channel of large relative roughness. *J. Hydraul. Res.* 14, 115-125.
- Bentham T., Britter R., 2003, Spatially averaged flow within obstacle arrays. *Atmos. Environ.* 37, 2037-2043.
- Berg P., Ry H., Janssen F., Meyer V., Jørgensen B.B., Huettel M., de Beer D., 2003, Oxygen uptake by aquatic sediments measured with a novel non-invasive eddy-correlation technique. *Mar. Ecol. Prog. Ser.* 261, 75-83.
- Blanchard M., 1997, Spread of the slipper limpet, *Crepidula fornicata* (L. 1758) in Europe. Current state and consequences. *Scient. Mar.* 61, 109-118.
- Castro I.P., Cheng H., Reynolds R., 2006, Turbulence over urban-type roughness: deductions from wind-tunnel measurements. *Bound. Layer Meteorol.* 118, 1, 109-131.
- Chapalain G., Thais L., 2000, Tide, turbulence and suspended sediment modelling in the eastern English Channel. *Coast. Eng.* 41, 295-316.
- Chauvaud L., 1998, La coquille Saint-Jacques en rade de Brest: un modèle biologique d'étude des réponses de la faune benthique aux fluctuations de l'environnement. Thèse doctorat Univ. Bretagne occidentale, Brest.
- Chauvaud L., Jean F., Ragueneau O., Thouzeau G., 2000, Long-term variation of the Bay of Brest ecosystem: benthic-pelagic coupling revisited. *Mar. Ecol. Prog. Ser.* 200, 35-48.
- Cheng H., Castro I.P., 2002, Near wall flow over urban-like roughness. *Bound. Layer Meteorol.* 104, 229-259.
- Coccal G.O., Thomas T.G., Castro I.P., Belcher S.E., 2006, Mean flow and turbulence statistics over groups of urban-like cubical obstacles. *Bound. Layer Meteorol.*, 121, 491-519.
- Criminaldi J.P., Thompson J.K., Rosman J.H., Lowe R.J., Koseff J.R., 2002, Physical-biological coupling in spore dispersal of kelp forest macroalgae. *Limnol. Oceanogr.* 47, 1137-1151.
- Engelund F., Fredse J., 1976, A sediment transport model for straight alluvial channels. *Nordic Hydrol.* 7, 293-306.
- Fincham, A., Delerce, G., 2000, Advanced optimization of correlation imaging velocimetry algorithms. *Exp. Fluids* 29, S013-S022.
- Fredse J., Andersen K.H., Sumer B.M., 1999, Wave plus current over a ripple-covered bed. *Coast. Eng.* 38, 177-221.
- Frésard M., Boncoeur J., 2006, Costs and benefits of stock enhancement and biological invasion control: the case of the Bay of Brest scallop fishery. *Aquat. Living Resour.* 19, 299-305.
- Gaylord B., Reed D.C., Washburn L., Raimondic P.T., 2004, Physical-biological coupling in spore dispersal of kelp forest macroalgae. *J. Mar. Syst.* 20, 49, 19-39.
- Godillot R., Caussade B., Ameziane T., Capblanq J., 2001, Interplay between turbulence and periphyton in rough open-channel flow. *J. Hydraul. Res.* 39, 3, 227-239.
- Grant W.D., Madsen O.S., 1982, Moveable bed roughness in unsteady oscillatory flows. *J. Geophys. Res.* 87, 469-481.
- Guérin L., 2004, La crépidule en rade de Brest: un modèle biologique d'espèce introduite proliférante en réponse aux fluctuations de l'environnement. Thèse doctorat, Univ. Bretagne occidentale, Brest.
- Guizien K., Dohmen-Janssen M., Vittori G., 2003, 1DV bottom boundary layer modeling under combined wave and current: suspension ejection events and phase lag effects. *J. Geophys. Res.* 108(C1), 3016, 1-15.
- Guizien K., 2005, Equilibrium bottom roughness of ripples derived from a 2DHV ripple model, In: L.C. van Rijn, R.L. Soulsby, P. Hoekstra, A.G. Davies (eds.), SANDPIT, Sand Transport and Morphology of Offshore Sand Mining Pits, Aqua Publications, The Netherlands, AB 1-9.
- Hamlyn D., Britter R., 2005, A numerical study of the flow field and exchange processes within a canopy of urban-type roughness. *Atmos. Environ.* 39, 3243-3254.
- Hughes S.A., Schwichtenberg B.R., 1998, Current-induced scour along a breakwater at Ventura Harbor. *Coast. Eng.* 34, 1-22.
- Jackson P.S., 1981, On the displacement height in the logarithmic velocity profile. *J. Fluid Mech.* 111, 15-25.
- Kamphuis J.W., 1974, Determination of sand roughness for fixed beds. *J. Hydraul. Res.* 12, 193-203.
- Kastner-Klein P., Plate E., Fedorovich E., 1997, Gaseous pollutant dispersion around urban-canopy elements: Wind tunnel case studies. *Internat. J. Environ. Pollut.* 8, 727-737.
- Kemp P.H., Simons R.R., 1982, The interaction between waves and a turbulent current: waves propagating with the current. *J. Fluid Mech.* 116, 227-250.
- Kemp P.H., Simons R.R., 1983, The interaction between waves and a turbulent current: waves propagating against the current. *J. Fluid Mech.* 130, 73-890.
- Kitaya Y., Shibuya T., Yoshida M., Kiyota M., 2004, Effects of air velocity on photosynthesis of plant canopies under elevated CO<sub>2</sub> levels in a plant culture system. *Adv. Space Res.* 34, 1466-1469.

- Kuo A. Y., Shen J., Hamrick J. M., 1996, Effect of acceleration on bottom shear stress in tidal estuaries. *J. Waterway, Port, Coastal, Ocean Eng.* 122, 75-83.
- Martin S., Thouzeau G., Chauvaud L., Jean F., Guérin L., Clavier J., 2006, Respiration, calcification, and excretion of the invasive limpet, *Crepidula fornicata* L.: Implications for carbon, carbonate, and nitrogen fluxes. *Limnol. Oceanogr.* 51, 5, 1996-2007.
- Martin S., Thouzeau G., Richard M., Chauvaud L., Jean F., Clavier J. Benthic community metabolism in areas impacted by the invasive species, *Crepidula fornicata* L., *Mar. Ecol. Prog. Series*, in press.
- McDonald R.W., 2000, Modelling the mean velocity profile in the urban canopy layer. *Bound. Layer Meteorol.* 97, 25-45.
- Orlandi P., Leonardi S., Antonia R.A., 2006, Turbulent channel flow with either transverse or longitudinal roughness elements on one wall. *J. Fluid Mech.* 561, 279–305.
- Peterson E.L., 1999, Benthic shear stress and sediment condition. *Aquac. Eng.* 21, 85-111.
- Prandtl L., 1925, Über die ausgebildete Turbulenz. *ZAMM* 5, 136-139.
- Ragueneau O., Chauvaud L., Leynaert A., Thouzeau G., Paulet Y.-M., Bonnet S., Lorrain A., Grall J., Corvaisier R., Le Hir M., Jean F., Clavier J., 2002, Direct evidence of a biologically active coastal silicate pump: ecological implications. *Limnol. Oceanogr.* 47, 6, 1849-1854.
- Ragueneau O., Chauvaud L., Moriceau B., Leynaert A., Thouzeau G., Donval A., Le Loc'h F., Jean F., 2005, Biodeposition by an invasive suspension feeder impacts the biogeochemical cycle of Si in a coastal ecosystem (Bay of Brest, France). *Biogeochemistry* 75, 19-41.
- Richard J., 2005, *Crepidula fornicata* L. : un modèle biologique pour l'étude du rôle de la variabilité des caractères phénotypiques (reproduction, croissance et nutrition) sur les processus de colonisation en milieu marin. Thèse doctorat Université Bretagne occidentale, Brest.
- Saffman P.G., 1970, A model for inhomogeneous turbulent flow. *Proc. R. Soc. Lond. A* 317, 417-433.
- Schlichting H., Gersten K., 2001, *Boundary layer theory* (Springer).
- Thouzeau G., Chauvaud L., Grall J., Guérin L., 2000, Rôle des interactions biotiques sur le devenir du pré-recrutement et la croissance de *Pecten maximus* (L.) en rade de Brest. *C. R. Acad. Sci. Paris, Sciences de la vie* 323, 815-825.
- Thouzeau G., Chauvaud L., Durand G., Patris T., Glémarec M., 2003, Impact des polluants d'origine anthropique sur les organismes benthiques marins: notions d'indicateurs biologiques de perturbation et de réseaux de surveillance. *Océanis* 27, 177-214.